ACS APPLIED MATERIALS & INTERFACES

Research Article

www.acsami.org

Enhanced Electron Field Emission Properties of Conducting Ultrananocrystalline Diamond Films after Cu and Au Ion Implantation

Kamatchi Jothiramalingam Sankaran,[†] Huang-Chin Chen,[‡] Kalpataru Panda,[§] Balakrishnan Sundaravel,[§] Chi-Young Lee,[†] Nyan-Hwa Tai,*[,†] and I-Nan Lin[‡]

[†]Department of Materials Science and Engineering, National Tsing-Hua University, Hsinchu 300, Taiwan, R.O.C.

[‡]Department of Physics, Tamkang University, Tamsui 251, Taiwan, R.O.C.

[§]Materials Science Group, Indira Gandhi Centre for Atomic Research, Kalpakkam 603 102, India

Supporting Information

ABSTRACT: The effects of Cu and Au ion implantation on the structural and electron field emission (EFE) properties of ultrananocrystalline diamond (UNCD) films were investigated. High electrical conductivity of 186 $(\Omega\bullet cm)^{-1}$ and enhanced EFE properties with low turn-on field of 4.5 V/μm and high EFE current density of 6.70 mA/cm^2 have been detected for Au-ion implanted UNCD (Au-UNCD) films that are superior to those of Cu-ion implanted UNCD (Cu-UNCD) ones. Transmission electron microscopic investigations revealed that Au-ion implantation induced a larger proportion of nanographitic phases at the grain boundaries for the Au-UNCD films in addition to the formation of uniformly distributed spherically shaped Au nanoparticles. In contrast, for Cu-UNCD films, plate-like Cu nanoparticles arranged in the row-like pattern were formed, and only a smaller proportion of nanographite phases along the grain boundaries was induced. From current imaging tunneling spectroscopy and local current−voltage curves of scanning tunneling spectroscopic measurements, it is observed that the electrons are dominantly emitted from the grain boundaries. Consequently, the presence of nanosized Au particles and the induction of abundant nanographitic phases in the grain boundaries of Au-UNCD films are believed to be the authentic factors, ensuing in high electrical conductivity and outstanding EFE properties of the films.

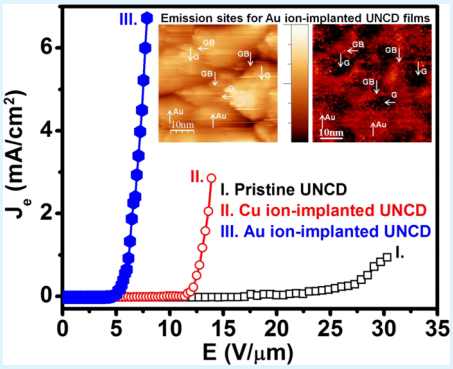

KEYWORDS: *ultrananocrystalline diamond films, ion implantation, nanographite, electron field emission, transmission electron microscopy, scanning tunneling spectroscopy*

INTRODUCTION

Diamond films have been examined extensively for their application as electron field emitters owing to their negative electron affinity and low effective work function.[1,2] Because of its excellent physical properties, such as high hardness, high surface acoustic wave velocity, high electron mobility, high thermal conductivity, and good chemical and thermal stability, there is considerable interest in the use of diamond as a semiconductor for the fabrication of high performance electronic devices applied in high temperature and heavy radiation environments.[3] Ultrananocrystalline diamond (UNCD) film is a special form of diamond film that has recently attracted increasing attention from researchers because of its exclusive granular structure.[4] The UNCD film has ultrasmall diamond grains (5−10 nm) and smooth surface characteristics. The grains of UNCD films have an sp^3 character and the grain boundaries have a mixture of sp^2, sp^3, hydrocarbon, and amorphous carbon (*a-C*), in which the sp^2 character is predominant.[5] Because of outstanding electron field emission (EFE) behavior from UNCD films as compared to other forms of diamond films (microcrystalline or nanocrystalline), UNCD films show large potential for applications such as cold cathode field emitters and other vacuum microelectronic devices.[6]

The high potential that the diamond or the UNCD films bears as a material for the fabrication of cold cathode emitting devices requires the films to be conductive. Incorporating N_2 into the growth plasma of UNCD films gives rise to a conversion of *a-C* phase to graphite phase at the grain boundaries, increasing the number of conduction paths in the material and hence improving the electrical conductivity and the EFE properties of the films.[7−10] However, N_2 incorporation via the addition of N_2 gas to the growth plasma requires high growth temperature (700 °C).[11,12]

On the other hand, ion implantation has long been utilized to tailor the properties of materials through controlled doping

Received: December 24, 2013
Accepted: March 13, 2014
Published: March 13, 2014

with the selection of dopants.[13−15] Ion implantation can break the C−C and hydrocarbon bonds to form sp^2 carbon. Moreover, compared with the surface modification process such as hydrogen plasma treatment on nanostructured diamond particles,[2] ion implantation modifies the diamond film to a larger depth, and enhanced EFE properties will last longer. Recent reports showed that oxygen,[16] phosphorous,[17] and nitrogen[18,19] ion implantation induce *a*-C phases in the grain boundaries of UNCD films which provide *n*-type conductivity. However, the electrical conductivity of *a*-C phases enclosed in the grain boundaries of UNCD films is not adequately high and, consequently, confines the EFE properties achievable for UNCD films. Hence, an ion implantation process, which can efficiently induce the graphitic phases in the grain boundaries of UNCD films to accomplish high conductivity, is thus called for.

In this paper, we reported the effects of Cu and Au ion implantations on enhancing the conductivity and EFE properties of UNCD films. We also investigated in depth the microstructural evolution of UNCD films induced by these ion implantation processes by using transmission electron microscopy (TEM). Moreover, we explored the mechanism on the enhanced EFE characteristics of ion implanted UNCD films from a microscopic viewpoint by using scanning tunneling microscopy (STM) and scanning tunneling spectroscopy (STS). The conducting regimes at both grains and grain boundaries were examined in detail. Most importantly, we demonstrated that the high EFE UNCD films developed in this paper have better potential for device applications, since both the processes for growing UNCD films and the ion implantation are simple, repeatable, robust, and scalable.

EXPERIMENTAL METHODS

The UNCD films were grown on *n*-type silicon substrates in a microwave plasma enhanced chemical vapor deposition (2.45 GHz IPLAS-CYRANNUS-I, Troisdorf, Germany) system. The substrates were ultrasonicated in methanol solution containing the mixture of diamond powders (about 4 nm in size) and titanium powders (SIGMA-ALDRICH; 365 mesh) for 45 min to facilitate the nucleation process. The UNCD films were grown in Ar(99%)/CH_4(1%) plasma (100 sccm), at 1200 W and 200 mbar for 3 h, without heating the substrate. The substrates were heated due to the bombardment of the plasma species and the substrate temperature was estimated to be around 475 °C during the growth of UNCD films. Ion implantation of the UNCD films was carried out in a 1.7 MV tandetran accelerator at room temperature and at pressure below 2×10^{-7} mbar with Au ions of 500 keV or Cu ions of 300 keV kinetic energy. Ion beam current for Au and Cu implantation was maintained at 220 nA, rastered over an aperture of 1 cm diameter which corresponds to a dose rate of 1.75×10^{12} ions/cm^2/s. The ion fluence of both Cu and Au ion implantations was 1×10^{17} ions/cm^2. SRIM2003 Monte Carlo program gives a projected ion range of 80 nm, straggling of 8.6 nm, electronic energy loss of 2876 eV/nm, and nuclear energy loss of 5070 eV/nm for 500 keV Au ions in diamond. 300 keV Cu ions in diamond show a projected ion range of 134 nm, straggling of 22 nm, electronic energy loss of 729 eV/nm, nuclear energy loss of 1320 eV/nm. Au ions deposit nearly three times the energy deposited by Cu ions. The Au and the Cu ion implanted UNCD films are designated as "Au-UNCD" and "Cu-UNCD", respectively.

The morphology and microstructure of the UNCD films were examined using field emission scanning electron microscopy (FESEM; JEOL 6500) and high resolution transmission electron microscopy (HRTEM; JEOL 2100F), respectively. The elemental distributions of the species in these films were examined using high angle annular dark field (HAADF) technique and three dimensional (3D)-tomography in scanning transmission electron microscopy mode. The 3D-tomography is the sequential replay of the HAADF images taken with the samples tilted step wisely (2°) using a software DIGITAL-MICROGRAPH (JEOL).[20] The crystalline quality and chemical bonding structures of the UNCD films were characterized by Raman spectroscopy (Lab Raman HR800, Jobin Yvon; λ = 632 nm) and X-ray photoelectron spectroscopy (XPS; PHI 1600), respectively.

Hall measurements were carried out in a van der Pauw configuration (ECOPIA HMS-3000) to observe the conducting behavior of these films. The EFE experiments were carried out using a homemade tunable parallel plate capacitor setup, where a molybdenum rod of 2 mm diameter was used as anode. The current density versus electrical field (J_e−E) characteristics were obtained using Keithley 2410 electrometer. The EFE properties of the materials were analyzed using the Fowler-Nordheim (F−N) theory.[21] The local electron emission behavior in the ion implanted UNCD films was investigated by ultra-high-vacuum STM (UHV STM; 150 Aarhus, SPECS GmbH, Germany). The STM tips were prepared by electrochemical etching of tungsten wires and the measurements were carried out at room temperature with a base pressure of 10^{-10} mbar. The STM imaging was performed with a constant current of 0.59 nA and a bias voltage of −5.0 V. Current imaging tunneling spectra (CITS) with voltages ramping from −5.0 to 5.0 V were measured concurrently during the STM image scanning at fixed height of tip over the examined region. A STS spectrum was computed from an average of many I−V curves taken at different positions in the STM image.

RESULTS AND DISCUSSION

A. Materials Characteristics. Figure 1a depicts the FESEM image of pristine UNCD films, revealing the nanometer scale of grain size with root-mean-square (rms) roughness of 0.7 nm, which were estimated from STM measurements (figure not shown). The cross-sectional FESEM image (inset of Figure 1a) reveals that the thickness

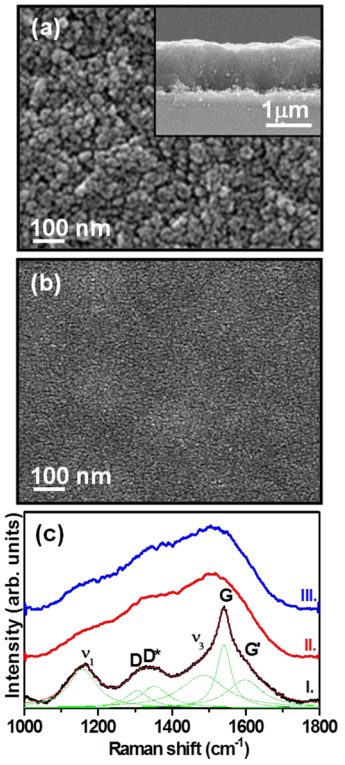

Figure 1. FESEM images of (a) pristine UNCD films with cross-section FESEM image shown as inset. (b) Typical morphology of Cu (or Au) ion implanted UNCD films. (c) Raman spectra of (I) pristine UNCD, (II) Cu-UNCD, and (III) Au-UNCD films.

of the pristine film is about 1.0 μm. After ion implantation, pronounced change in the surface morphology is evident. The equi-axed granular structure of the pristine UNCD films was changed into featureless surface morphologies for both Cu-UNCD and Au-UNCD films as illustrated in Figure 1b. Figure 1c shows the Raman spectra of pristine UNCD films, Cu-UNCD films, and Au-UNCD films. The Raman spectra were deconvoluted by using the multi-peak Lorentzian fitting method. Six peaks were observed in pristine UNCD films which were designated as ν_1 (1162 cm^{-1}), ν_3 (1482 cm^{-1}), D (1306 cm^{-1}), D* (1353 cm^{-1}), G (1539 cm^{-1}), and G′ (1594 cm^{-1}) as illustrated in curve I of Figure 1c. The D-band resonance peak at 1306 cm^{-1} is the characteristic of diamond phase. ν_1 at 1162 cm^{-1} and ν_3 at 1482 cm^{-1} are the peaks attributed to the *trans*-polyacetylene (*t*-PA) phases present in the grain boundaries of UNCD films.[22] Moreover, D*-band (1353 cm^{-1}) and G-band (1539 cm^{-1}) represent the disordered and ordered carbons, i.e., the *a*-C and graphitic content in the UNCD films, respectively.[23−25] A shoulder peak at 1594 cm^{-1} (designated as G′ band) is seen that possibly arises from the nanocrystalline graphitic content of the UNCD films. The effects of Cu and Au ion implantation on altering the bonding characteristics of UNCD films are shown as curves II and III of Figure 1c. The higher intensities of D* and G peaks in curves II and III of Figure 1c indicate, respectively, amorphization and graphitization types of transitions in the UNCD films due to ion implantation. It is to be noted that visible-Raman spectroscopy can only give information on sp^2-bonded carbon and indirect information regarding sp^3 content. More detailed investigation on the phase constituents contained in the UNCD films will be illustrated by TEM shortly.

The C1s photoemission spectra of the XPS measurements for the UNCD films are shown in Figure 2. The background was subtracted by using Shirley's method.[26] The measurement was conducted without ion sputtering etching to avoid reconfiguration of the bonds. The data are fitted with Lorentzian peaks with binding energies at 284.4, 285.0, and 287.0 eV corresponding to sp^2 C═C, sp^3 C—C, and CO/C—O—C bonds, respectively, and their relative intensities are tabulated in Table 1. In pristine UNCD films, sp^3 C—C bonding is predominant with a peak intensity of 67.5%, while sp^2 C═C intensity is 27.9% (Figure 2a). The CO/C—O—C peak is seen with an intensity of 3.6% at binding energy of 287 eV, and it disappears if surface is ion sputtering etched. After Cu-ion implantation, sp^3 C—C peak intensity decreases to 47.0% and sp^2 C═C peak intensity increases to 45.4% (Figure 2b). Moreover, the Au-UNCD films shows the sp^3 C—C peak of 25.4% with sp^2 C═C peak intensity of 71.5% (Figure 2c). The increase in sp^2 content upon Cu- (or Au-) ion implantation is consistent with our Raman data (cf. Figure 1c).

B. Electrical Properties. The Hall measurements in van der Pauw configuration indicates that, while the resistivity of the pristine UNCD films is too large to be measurable by van der Pauw configuration, the Cu-UNCD films possess the electrical conductivity of σ = 0.07 Ω•cm^{-1} with sheet carrier concentration of $n = 1.3 \times 10^{14}$ cm^{-2} and mobility of $\mu = 0.3 \times 10^2$ cm^2/V•s. Interestingly, the higher conductivity of 186 Ω•cm^{-1} with $n = 5.5 \times 10^{20}$ cm^{-2} and $\mu = 8.5 \times 10^2$ cm^2/V•s is achieved for Au-UNCD films.

Figure 3 shows the enhancement in the EFE properties of UNCD films due to ion implantation, whereas the inset shows the F−N plot, the variation of ln (J_e/E^2) versus 1/E, of the corresponding field emission data. The turn-on field (E_0) was

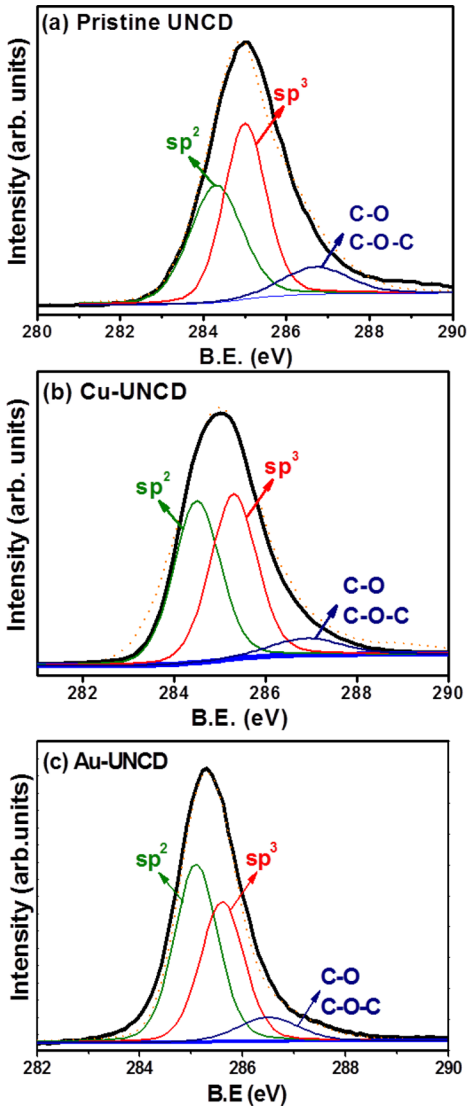

Figure 2. C1s XPS spectra from (a) pristine UNCD, (b) Cu-UNCD, and (c) Au-UNCD films.

Table 1. Relative Intensities of Various Components of C1s XPS Spectra for the Cu and Au Ion Implanted UNCD Films

	chemical bonding (%)		
samples	sp^2 C═C (284.4)	sp^3 C−C (285.0)	CO/C−O−C (287.0)
Pristine UNCD	27.9	67.5	3.6
Cu-UNCD	45.4	47.0	7.6
Au-UNCD	71.5	25.4	3.1

assigned as the interception of the straight lines extrapolated from the low field and high field segments of the F−N plots. The E_0 value for inducing EFE process decreased from 16.2 V/μm for pristine UNCD films (curve I, Figure 3) to 7.9 V/m for Cu-UNCD films (curve II, Figure 3), whereas the J_e value increased from 0.96 mA/cm^2 at an applied field of 30.3 V/μm for pristine UNCD films to a value of 2.86 mA/cm^2 (at an applied field of 13.8 V/μm) for Cu-UNCD films. The EFE properties are even better for the Au-UNCD films, viz., with the smallest E_0 value of 4.5 V/μm and the highest J_e value of 6.7 mA/cm^2 at an applied field of 7.8 V/μm (curve III, Figure 3). Moreover, the effective work function, φ_{eff}, is defined as φ/β,

dx.doi.org/10.1021/am405954w | ACS Appl. Mater. Interfaces 2014, 6, 4911−4919

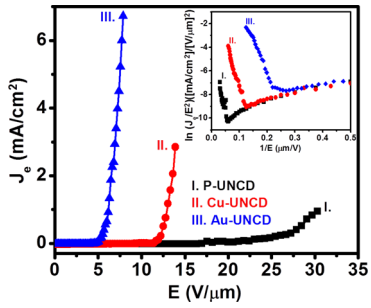

Figure 3. Electron field emission properties (J_e–E curves) of (I) pristine UNCD, (II) Cu-UNCD, and (III) Au-UNCD films. The inset shows the corresponding Fowler-Nordheim plots.

where φ is the work function of the diamond materials and β is the field enhancement factor of the emission sites; φ_{eff} values of these UNCD films calculated from the slope of the F–N plots show that the φ_{eff} values of these UNCD films are $\varphi_{pristine\ UNCD}$ = 0.0205 eV, $\varphi_{Cu\text{-}UNCD}$ = 0.0173 eV, and $\varphi_{Au\text{-}UNCD}$ = 0.0155 eV. However, the difference in φ_{eff} values is not very large and does not seem to be the prime factor altering the EFE properties of these films. The details of the electrical conductivity, the effective work function, and the EFE properties of the pristine and the Au- (or Cu-) ion implanted UNCD films are listed in Table 2, where those parameters of the UNCD films implanted with other kinds of species were included to facilitate the comparison. Notably, both the Au-UNCD and the Cu-UNCD films show overwhelmingly better electrical conductivity and EFE characteristics than those of other diamond based field emitting materials (see Table 2).[2,10,16,17,27] These results indicate that the improvement of the EFE properties of the ion implanted films is closely related to the enhancement in the electrical properties of the films that, in turn, is owed to the increase in the proportion of the sp^2-bonded carbon in these films. The change in the φ_{eff} values does not seem to be the prime factor altering the EFE properties for the UNCD films.

C. Scanning Tunneling Spectroscopy. The local EFE properties of the films were investigated by CITS mode in STS to directly reveal the distribution of the emission sites in these films. Notably, only the high conductivity Au-UNCD (Cu-UNCD) films show prominent signals in CITS (STS) mode and the pristine UNCD films are too high in resistivity for STS measurements. Figure 4a shows the high resolution STM (HRSTM) image of Cu-UNCD films. The grains are of nanometer size and the rms roughness is found to be ~0.6 nm. The typical grains and grain boundaries are marked as 'G' and 'GB', respectively. Figure 5a shows the CITS image corresponding to Figure 4a taken at a sample bias of −5.0 V, where the bright spots represent large emission current and vice versa. Bright and dark regions in CITS image are visible with their shapes resembling the shapes of GB and G of the HRSTM image shown in Figure 4a, respectively. The CITS image depicted in Figure 5a shows evidently that the electrons are mostly emitted from the GBs (bright regions) rather than grains. In contrast, Figure 4b shows the HRSTM image of Au-UNCD films. The grain size and the rms roughness are almost the same as those of the Cu-UNCD films. The CITS image taken at a sample bias of −5.0 V corresponding to Figure 4b is shown in Figure 5b, revealing again that the GBs are the prominent electron emission sites in comparison to that of the grains. It is to be noted that some large clusters in the Au-UNCD films also emit like the GBs, which may be from the carbon-coated Au nanoparticles which are residually present on the surface of the Au-UNCD films and are thus marked 'Au' in Figure 5b. Moreover, in comparison with the CITS image of Cu-UNCD films, it is clearly evident that the emission sites

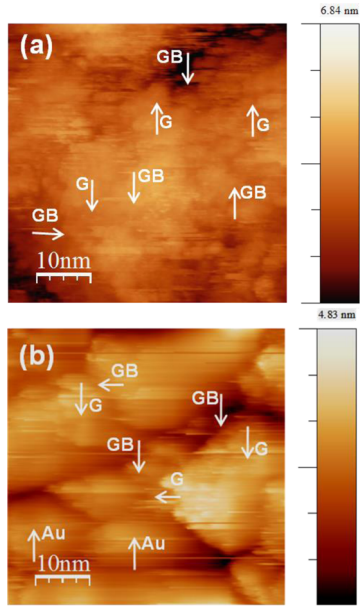

Figure 4. HRSTM images of (a) Cu-UNCD films and (b) Au-UNCD films. The typical grains and grain boundaries are marked as 'G' and 'GB', respectively.

Table 2. Comparison of Electrical and Electron Field Emission Properties of Cu and Au Ion Implanted UNCD Films with Other Species in Diamond Films

samples	sheet carrier concentration (cm^{-2})	mobility (cm^2/V• s)	conductivity (Ω •cm)$^{-1}$	turn-on field (V/μm)	EFE current density (mA/cm^2)	effective work function (eV)
Pristine UNCD	---	---	---	16.2	0.96 @ 30.3 V/μm	0.0205
Cu-UNCD	1.3×10^{14}	0.3	0.07	7.9	2.86 @ 13.8 V/μm	0.0173
Au-UNCD	5.5×10^{20}	8.5	186	4.5	6.70 @ 7.8 V/μm	0.0155
H-treated diamond[2]	---	---	---	1.5	1 $\mu A/cm^2$ @ 1.5 V/μm	---
N-doped UNCD[10]	2×10^{22}	---	185	6.13	3.36 @ 8.8 V/μm	---
O-implanted UNCD[16]	10^{16}	11	33.3	---	---	---
P-implanted UNCD[17]	10^{17}	143	0.09	---	---	---
Li-doped UNCD[27]	3.6×10^{13}	---	7.4×10^{-3}	12	0.20 @ 20.0 V/μm	---

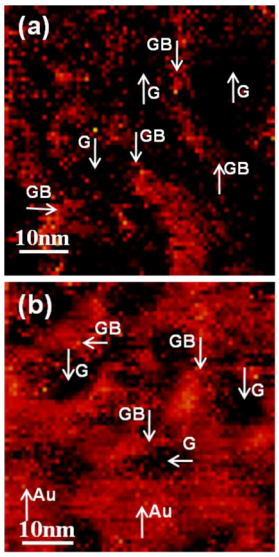

Figure 5. CITS image of (a) Cu-UNCD films corresponding to the STM image of Figure 4a and (b) Au-UNCD films corresponding to the STM image of Figure 4b. The typical grains and grain boundaries are marked as 'G' and 'GB', respectively.

(bright regions) are more abundant for Au-UNCD films (cf. Figure 5a and b).

Moreover, *I*−*V* curves were taken from STM at various local positions of grains and grain boundaries corresponding to the STM images shown in Figure 4a and b, respectively, for Cu-UNCD and Au-UNCD films and are shown in Figure 6a and b, respectively. Only the negative portion of the *I*−*V* curves, which indicated the emission of electrons from the films, was shown here. Reproducible *I*−*V* curves were recorded during the

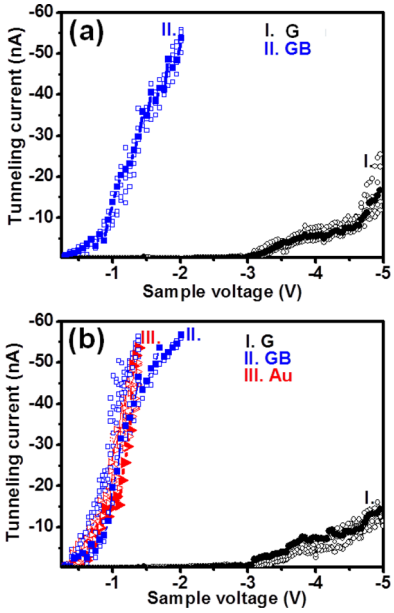

Figure 6. (a) Local *I*−*V* characteristic curves at the (I) grain (G, solid circles) and (II) grain boundary (GB, solid squares) of Cu-UNCD films. (b) Local *I*−*V* characteristic curves at the (I) grain (G, solid circles), (II) grain boundary (GB, solid squares), and (III) Au clusters (Au, solid triangles) of Au-UNCD films. The reproducible *I*−*V* spectra (10 each) are shown by open symbols and the average of these curves is plotted as solid symbols.

scanning of these UNCD films. The reproducible *I*−*V* curves (10 each) were shown in open symbols and the average of these curves was plotted as solid symbols. We observed a significant difference in the *I*−*V* characteristic curve at grain and grain boundary for both samples. The grain boundaries (GBs, curve II (solid squares) of Figure 6a and b) emit electrons better than the grains (G, curve I (solid circles) of Figure 6a and b). The grain boundaries of Au-UNCD films (curve II (solid squares), Figure 6b) emit electrons at a lower threshold bias as compared to that of the grain boundaries of Cu-UNCD films (curve II (solid squares), Figure 6a). Additionally, the Au residual presence on the surface of Au-UNCD films, marked as 'Au' in the CITS image of Figure 5b, also showed lower threshold bias (curve III (solid triangles), Figure 6b) as the grain boundaries of Au-UNCD films (curve II (solid squares), Figure 6b). Consequently, the Au-UNCD films not only show more bright emission sites in the grain boundaries as compared with those of Cu-UNCD films (cf. Figure 5a and b), but in addition, the grain boundaries of Au-UNCD films emitted larger STS current than that of the Cu-UNCD films. Such an observation is in accord with the enhanced electrical conductivity and EFE behavior of the Au-UNCD films as compared to that of Cu-UNCD films.

D. Transmission Electron Microscopy. The STS measurements clearly illustrate the benefit of Au-ion implantation on increasing the number density of field emission sites as compared with the Cu-ion implantation on UNCD films. However, the authentic factor for such an effect is still not clear. It is expected that the modification of the granular structure for these films due to ion implantation is the key. To investigate the possible cause of such phenomena, the detailed microstructure of these films was examined using TEM. Notably, in the preparation of TEM thin foil, the samples were ion milled from both the top and bottom surfaces at the same time, such that the TEM samples mainly contain the materials in the interior region of the UNCD films, where the implanted ions reside. Figure 7 shows the TEM microstructure of pristine UNCD, Cu-UNCD, and Au-UNCD films with the corresponding selected area electron diffraction (SAED) patterns shown as insets. The pristine UNCD films contain nanosized clusters, which are uniformly distributed (Figure 7a). The corresponding SAED pattern (inset, Figure 7a) contains sharp diffraction rings corresponding to (111), (220), and (311) diamond lattices, which confirms that the nanosized clustered grains are of diamond structure. There appears to be a diffused ring in the center of the SAED, indicating the existence of the *t*-PA phase located in the grain boundaries of the films. There is no more diffraction other than diamond observable.

The TEM bright field images of Cu-UNCD and Au-UNCD films were shown in Figure 7b and c, respectively, which clearly show the presence of nanosized clusters, besides the diamond grains. The SAED pattern for Cu-UNCD films shown as inset in Figure 7b illustrates that, besides the diffraction rings corresponding to diamond lattice planes, there is an extra diffraction ring, corresponding to Cu material with lattice spacing of 0.208 nm that is located outside the (111) diamond ring, which has lattice spacing of 0.206 nm. Likewise, the SAED pattern for Au-UNCD films (inset, Figure 7c) also illustrates an extra diffraction ring located inside the (111) diamond ring with the lattice spacing of 0.235 nm, which corresponds to Au materials. Such observations confirm that the clusters contained in the Cu-UNCD (Figure 7b) and Au-UNCD films (Figure 7c) are nanosized Cu and Au particles, respectively. The presence

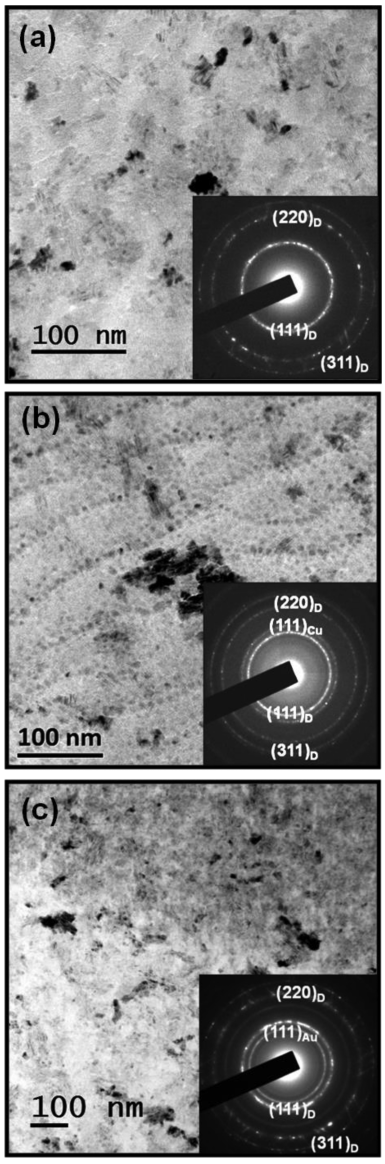

Figure 7. TEM micrographs for (a) pristine UNCD, (b) Cu-UNCD, and (c) Au-UNCD films with the insets showing the corresponding SAED pattern.

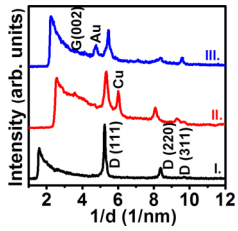

Figure 8. Linear diffraction patterns (LDP) derived from the SAED patterns shown in Figure 7a–c, corresponding to (curve I) pristine UNCD, (curve II) Cu-UNCD, and (curve III) Au-UNCD films.

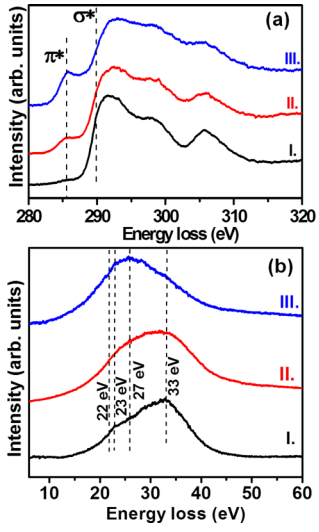

Figure 9. Selected area EELS spectroscopy of UNCD films: (a) core-loss EELS spectra and (b) plasmon-loss EELS spectra, where (I) is pristine UNCD corresponding to Figure 7a, (II) is Cu-UNCD corresponding to Figure 7b, and (III) is Au-UNCD films corresponding to Figure 7c.

of Cu and Au impurities in the respective UNCD films was also confirmed by the EDAX patterns, which is shown in Figure S3. Diffused rings in the center of the SAED patterns are also found (insets of Figure 7b and c), which indicate the presence of *a*-*C* or graphite in these films. The phase constituents contained in the UNCD films are more clearly demonstrated by the linear diffraction patterns (LDP) (Figure 8), which were derived from the corresponding SAED patterns in the insets of Figure 7a to c. The LDP of these films reveal clearly that, while the pristine films (curve I) contain mainly the diamond, the Cu-UNCD films contain an extra diffraction peak corresponding to Cu (curve II) and the Au-UNCD films contain the extra diffraction peak corresponding to Au (curve III), besides the central diffuse peaks corresponding to graphite or *a*-*C* phase.

Moreover, selective area electron energy loss spectroscopy (EELS) spectra (Figure 9) were recorded in the carbon K-edge region to unambiguously distinguish between the diamond and non-diamond phases contained in the ion implanted UNCD films.[28] The core-loss EELS spectrum of pristine UNCD films, corresponding to TEM image in Figure 7a, is shown as curve I in Figure 9a, which exhibits typical EELS spectrum of diamond with *Fd*3*m* structure, as they contain an abrupt rise in σ^*-band (near 290 eV) and a large valley near 302 eV.[29,30] The σ^*-band for the UNCD films is not as sharp as the spectra for microcrystalline diamond films[31] that is ascribed to the presence of a large proportion of surface for the ultrasmall diamond grains in UNCD films, as the surface contains larger proportion of distorted sp^3-bonds. The core-loss EELS spectra of Cu-UNCD films (curve II, Figure 9a) is essentially the same as those of the pristine UNCD films, whereas those of Au-UNCD films (curve III, Figure 9a) were largely distorted, implying that the diamond lattices (sp^3-bonded carbons) in Au-UNCD films were heavily defected. Moreover, there is a prominent π^*-band at 285 eV in core-loss EELS for Cu-UNCD and Au-UNCD films but not visible in pristine UNCD films, indicating the presence of sp^2-bonded carbon in the grain boundary regions of Cu-UNCD and Au-UNCD materials. These observations are in accord with our Raman and XPS analyses (cf. Figures 1c and 2c). Moreover, the Cu core-loss EELS spectrum in the 920–1000 eV regimes of Cu-UNCD films corresponding to TEM image in Figure 7b, which were shown as Figure S4a, revealed a peak at 934 eV, confirming the presence of Cu-clusters in the Cu-UNCD films.[32] Likewise, the Au core-loss EELS spectrum in 45–200 eV regimes of Au-UNCD films corresponding to TEM image in Figure 7c, which

were shown as Figure S4b, illustrated a peak at 56 eV, which authenticates the presence of Au-clusters in the Au-UNCD films.[33]

Now the question yet to be solved is what kind of grain boundary phases (*a*-*C* or graphite) were induced when the UNCD films were implanted using Cu or Au ions. It should be mentioned that the plasmon-loss EELS spectra is the most effective measurement to differentiate the crystalline sp^2-bonded carbons (the graphite) from the amorphous one, as the plasmon-loss EELS spectra for the graphitic phase shows a prominent peak at s_3 (27 eV) and the *a*-*C* phase shows a peak at s_1 (22 eV),[30,34] whereas the crystalline sp^3-bonded carbon, the diamond, shows a peak corresponding to the bulk plasmon loss at s_4 (33 eV) with a shoulder corresponding to the surface plasmon loss at s_2 (23 eV). The I_{s2}/I_{s4} ratio is about $1:\sqrt{2}$. Figure 9b shows the plasmon-loss EELS spectra of the same regions. It is observed that the pristine UNCD films (curve I, Figure 9b) is dominated by s_2 and s_4 peaks, indicating that pristine UNCD films are diamond.[34] Curve II of Figure 9b shows the plasmon-loss EELS spectrum of Cu-UNCD films, which indicates that s_2- and s_4-bands still dominate but with increased spectral weight of s_3-band (27 eV) as compared to that of curve I. This result indicates that Cu-ion implantation causes increased content in nanographite phases as compared with the pristine UNCD films. Quite the opposite, the plasmon-loss spectrum for Au-UNCD film (curve III, Figure 9b) is dominated by larger s_3-band (~27 eV) with the s_2- and s_4-bands of much smaller intensity, indicating that this region consists of even larger proportion of graphitic phases besides diamond that is in accord with the core-loss spectrum of Au-UNCD films.

To understand the authentic factor that enhanced the EFE behavior for the Au-UNCD and Cu-UNCD films, the more detailed microstructural information, such as the geometry and distribution of the Cu and Au nanoparticles, was examined using the HAADF technique and 3D-tomography in TEM, which was the sequential replay of the HAADF images taken with the samples tilted stepwise (2°). The videos illustrating the 3D-tomograph of the Cu-UNCD and Au-UNCD films are shown as videos S1 and S2, respectively. Figure 10a shows the stereographic projection of the 3D-tomography for the Cu-UNCD films, whereas Figure 10b shows the *X*-*Y* projection of this image. These micrographs illustrate clearly that the Cu nanoparticles (red color) are of plate-like geometry and are arranged as rows among the UNCD films. In contrast, the stereographic projection of the 3D-tomography (Figure 11a) and *X*-*Y* projection of Au-UNCD films (Figure 11b) illustrate that the Au nanoparticles (yellow color) are of spherical geometry and are uniformly distributed among the diamond grains.

From the EELS results, we observe clearly that, while both the Cu- and Au-ion implantation can induce graphitic phases in the grain boundaries of UNCD films, the Au-ion implantation induced more abundant graphitic phases in the grain boundaries of Au-UNCD films, which assists the electron transport and results in more emission sites, as illustrated in the CITS measurements (cf. Figure 5b). These observations support the arguments that the uniform distribution of Au nanoparticles and the induction of graphitic phases among the diamond grains form an interconnected conducting network that facilitates the electron transport, resulting in better electrical conductivity and superior EFE properties for Au-UNCD films. Such observations are in accord with our previous

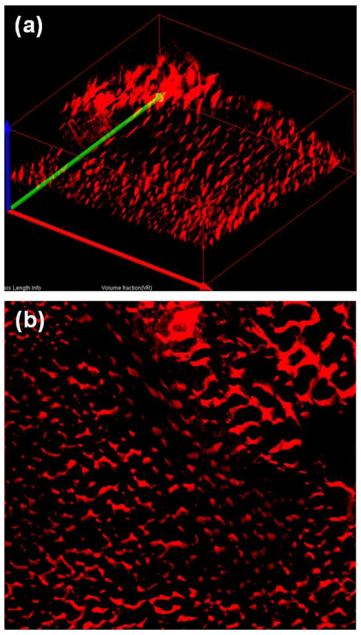

Figure 10. (a) Stereographic projection and (b) *X*-*Y* projection of the TEM 3D-tomography of Cu-UNCD films, showing the distribution of Cu clusters in these films (the video showing the 3D-tomography of the Cu-UNCD films is included as Video S1 in Supporting Information).

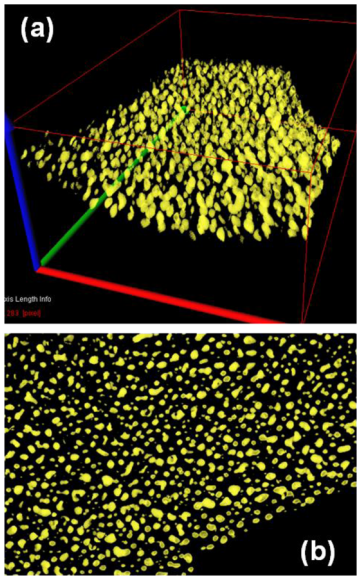

Figure 11. (a) Stereographic projection and (b) *X*-*Y* projection of the TEM 3D-tomography of Au-UNCD films, showing the distribution of Au clusters in these films (the video showing the 3D-tomography of the Au-UNCD films is included as Video S2 in Supporting Information).

reports that the grain boundary phases (*a*-*C* or graphite) existing among the diamond grains of the UNCD films are one of the genuine factors for the enhancement in electrical conductivity and EFE properties of UNCD films.[35] It is to be noted that the electron conductivity of the *a*-*C* grain boundary phases of UNCD films is not sufficiently high as compared with the graphitic phase, therefore restraining the EFE properties attainable for UNCD films.[16,17]

Concerning the different behavior for the implanted Cu- and Au-ions in enhancing the formation of nanographite phase, the genuine mechanism is not well understood yet. The Cu materials seem to have solubility to the carbon, although it is of limited value, as the Cu foil can be used to grow graphene in the chemical vapor deposition process.[36] Apparently, such a limited Cu-to-carbon interaction is the cause, inducing the formation of plate-like clusters in Cu-UNCD films. The dissolution and reprecipitation process tend to form *a-C*. In contrast, the phenomenon in which the implanted Au-ions form spherically shaped nanoparticles implies that there is essentially no solubility for the Au materials to the carbon. However, it has been observed in some organometallic compounds that the presence of Au species can catalytically convert the sp^3 hybridization to sp^2 hybridization.[37] Presumably, it is the catalyst effect of nanosized Au particles that caused the implanted Au-ions to induce a large proportion of nanographitic phase in UNCD films. However, such an argument requires more detailed investigation.

CONCLUSIONS

In summary, Cu and Au ion implantation markedly modified the microstructure and EFE properties of UNCD films. In Cu-UNCD films, the Cu nanoparticles were arranged in rows with plate-like geometry and a smaller amount of nanographitic phases was induced in the grain boundaries of the UNCD films that resulted in fewer emission sites in the CITS measurements, exhibiting less enhancement of EFE properties for the films. On the other hand, Au-ion implantation formed uniformly distributed spherically shaped Au nanoparticles and induced more abundant nanographitic phases in the grain boundaries of the UNCD films. These nanographites contain in the grain boundaries of Au-UNCD films form highly conductive channels at the interface of UNCD grain. These channels give rise to prominent electron emission from the grain boundaries resulting in high electrical conductivity and enhanced EFE properties for the Au-UNCD films. The highly conducting Au-UNCD films with better EFE characteristics open up an alleyway to the next generation of electron field emitters for applications in high-definition flat panel displays or plasma illumination devices.

ASSOCIATED CONTENT

Supporting Information

Videos showing 3D tomography of Cu-UNCD and Au-UNCD films. TEM micrographs. EELS spectroscopy. This material is available free of charge via the Internet at http://pubs.acs.org.

AUTHOR INFORMATION

Corresponding Author

*E-mail: nhtai@mx.nthu.edu.tw.

Notes

The authors declare no competing financial interest.

ACKNOWLEDGMENTS

The authors thank the financial support of National Science Council through the project nos. NSC 101-2221-E-007-064-MY3 and NSC 102-2112-M-032-006.

REFERENCES

(1) Himpsel, F. J.; Knapp, J. A.; VanVecten, J. A.; Eastman, D. E. Quantum Photoyield of Diamond(111)- A Stable Negative Affinity Emitter. *Phys. Rev. B* **1979**, *20*, 624−627.

(2) Zhu, W.; Kochanski, G. P.; Jin, S. Low-Field Electron Emission from Undoped Nanostructured Diamond. *Science* **1998**, *282*, 1471−1473.

(3) Tsubota, T.; Fukui, T.; Saito, T.; Kusakabe, K.; Morooka, S.; Maeda, H. Surface Morphology and Electrical Properties of Boron-doped Diamond Films Synthesized by Microwave-assisted Chemical Vapor Deposition using Trimethylboron on Diamond (100) Substrate. *Diamond Relat. Mater.* **2000**, *9*, 1362−1368.

(4) Corrigan, T. D.; Gruen, D. M.; Krauss, A. R.; Zapol, P.; Chang, R. P. H. The Effect of Nitrogen Addition to Ar/CH_4 Plasmas on the Growth, Morphology and Field emission of Ultrananocrystalline Diamond. *Diamond Relat. Mater.* **2002**, *11*, 43−48.

(5) Birrell, J.; Carlisle, J. A.; Auciello, O.; Gruen, D. M.; Gibson, J. M. Morphology and Electronic Structure in Nitrogen-doped Ultrananocrystalline Diamond. *Appl. Phys. Lett.* **2002**, *81*, 2235−2237.

(6) Sankaran, K. J.; Joseph, P. T.; Chen, H. C.; Tai, N. H.; Lin, I. N. Investigation in the Role of Hydrogen on the Properties of Diamond Films Grown using $Ar/H_2/CH_4$ Microwave Plasma. *Diamond Relat. Mater.* **2011**, *20*, 232−237.

(7) Zhou, D.; Krauss, A. R.; Qin, L. C.; McCauley, T. G.; Gruen, D. M.; Corrigan, T. D.; Chan, R. P. H.; Gnaser, H. Synthesis and Electron Field Emission of Nanocrystalline Diamond Thin Films Grown from N_2/CH_4 Microwave Plasmas. *J. Appl. Phys.* **1997**, *82*, 4546−4450.

(8) Birrell, J.; Gerbi, J. E.; Auciello, O.; Gibson, J. M.; Gruen, D. M.; Carlisle, J. A. Bonding Structure in Nitrogen Doped Ultrananocrystalline Diamond. *J. Appl. Phys.* **2003**, *93*, 5606−5612.

(9) Arenal, R.; Bruno, P.; Miller, D. J.; Bleuel, M.; Lal, J.; Gruen, D. M. Diamond Nanowires and the Insulator-Metal Transition in Ultrananocrystalline Diamond Films. *Phys. Rev. B* **2007**, *75*, No. No.195431.

(10) Sankaran, K. J.; Kurian, J.; Chen, H. C.; Dong, C. L.; Lee, C. Y.; Tai, N. H.; Lin, I. N. Origin of a Needle-like Granular Structure for Ultrananocrystalline Diamond Films Grown in a N_2/CH_4 Plasma. *J. Phys. D: Appl. Phys.* **2012**, *45*, No. No. 365303.

(11) Bhattacharyya, S.; Auciello, O.; Birrell, J.; Carlisle, J. A.; Curtiss, L. A.; Goyette, A. N.; Gruen, D. M.; Krauss, A. R.; Schlueter, J.; Sumant, A.; Zapol, P. Synthesis and Characterization of Highly-conducting Nitrogen-doped Ultrananocrystalline Diamond Films. *Appl. Phys. Lett.* **2001**, *79*, 1441−1443.

(12) Lin, Y. C.; Sankaran, K. J.; Chen, Y. C.; Lee, C. Y.; Chen, H. C.; Lin, I. N.; Tai, N. H. Enhancing Electron Field Emission Properties of UNCD films Through Nitrogen Incorporation at High Substrate Temperature. *Diamond Relat. Mater.* **2011**, *20*, 191−195.

(13) Kalish, R. Doping of Diamond. *Carbon* **1999**, *37*, 781−785.

(14) Talapatra, S.; Cheng, J. Y.; Chakrapani, N.; Trasobares, S.; Cao, A.; Vajtai, R.; Huang, M. B.; Ajayan, P. M. Ion Irradiation Induced Structural Modifications in Diamond Nanoparticles. *Nanotechnology* **2006**, *17*, 305−309.

(15) Prawer, S.; Kalish, R. Ion-beam-induced Transformation of Diamond. *Phys. Rev. B* **1995**, *51*, 15711−15722.

(16) Hu, X. J.; Ye, J. S.; Liu, H. J.; Shen, Y. G.; Chen, X. H.; Hu, H. n-type Conductivity and Phase Transition in Ultrananocrystalline Diamond Films by Oxygen Ion Implantation and Annealing. *J. Appl. Phys.* **2011**, *109*, No. No. 053524.

(17) Hu, X. J.; Ye, J. S.; Hu, H.; Chen, X. H.; Shen, Y. G. Phosphorus Ion Implantation and Annealing Induced n-type Conductivity and Microstructure Evolution in Ultrananocrystalline Diamond Films. *Appl. Phys. Lett.* **2011**, *99*, No. No. 131902.

(18) Joseph, P. T.; Tai, N. H.; Lee, C. Y.; Niu, H.; Pong, W. F.; Lin, I. N. Field Emission Enhancement in Nitrogen-ion-implanted Ultrananocrystalline Diamond Films. *J. Appl. Phys.* **2008**, *103*, No. No.043720.

(19) Panda, K.; Sundaravel, B.; Panigrahi, B. K.; Magudapathy, P.; Nandagopala Krishna, D.; Nair, K. G. M.; Chen, H. C.; Lin, I. N. Structural and Electronic Properties of Nitrogen Ion Implanted Ultra

Nanocrystalline Diamond Surfaces. *J. Appl. Phys.* **2011**, *110*, No. No. 044304.
(20) For information on Digital Micrograph (JEOL) software, see http://www.jeolusa.com/RESOURCES/ElectronOptics/DocumentsDownloads/tabid/320/Default.aspx?EntryId=800.
(21) Fowler, R. H.; Nordheim, L. Electron Emission in Intense Electric Fields. *Proc. R. Soc. London, Ser. A* **1928**, *119*, 173−181.
(22) Ferrari, A. C.; Robertson, J. Origin of the 1150−cm^{-1} Raman mode in Nanocrystalline Diamond. *Phys. Rev. B* **2001**, *63*, No. No. 121405.
(23) Michler, J.; Von Kaenel, Y.; Stiegler, J.; Blank, E. Complementary Application of Electron Microscopy and Micro-Raman Spectroscopy for Microstructure, Stress, and Bonding Defect Investigation of Heteroepitaxial Chemical Vapor Deposited Diamond Films. *J. Appl. Phys.* **1998**, *83*, 187−197.
(24) Ferrari, A. C.; Robertson, J. Interpretation of Raman Spectra of Disordered and Amorphous Carbon. *Phys. Rev. B* **2000**, *61*, 14095−14107.
(25) Ilie, A.; Ferrari, A. C.; Yagi, T.; Rodil, S. E.; Robertson, J.; Barborini, E.; Milani, P. Role of sp^2 Phase in Field Emission from Nanostructured Carbons. *J. Appl. Phys.* **2001**, *90*, 2024−2032.
(26) Chen, Y. F. Monte Carlo Simulation of Photoelectron Angular Distribution. *Surf. Sci.* **1997**, *380*, 199−209.
(27) Thomas, J. P.; Chen, H. C.; Tai, N. H.; Lin, I. N. Freestanding Ultrananocrystalline Diamond Films with Homojunction Insulating Layer on Conducting Layer and Their High Electron Field Emission Properties. *ACS Appl. Mater. Interfaces* **2011**, *3*, 4007−4013.
(28) Dato, A.; Radmilovic, V.; Lee, Z.; Philips, J.; Frenklach, M. Substrate-Free Gas-Phase Synthesis of Graphene Sheets. *Nano Lett.* **2008**, *8*, 2012−2016.
(29) Gruen, D. M.; Liu, S.; Krauss, A. R.; Luo, J.; Pan, X. Fullerenes as Precursors for Diamond Film Growth without Hydrogen or Oxygen Additions. *Appl. Phys. Lett.* **1994**, *64*, 1502−1504.
(30) Kovarik, P.; Bourdon, E. B. D.; Prince, R. H. Electron-energy-loss Characterization of Laser-deposited *a*-C, *a*-C:H, and Diamond Films. *Phys. Rev. B* **1993**, *48*, 12123−12129.
(31) Chen, S. S.; Chen, H. C.; Wang, W. C.; Lee, C. Y.; Lin, I. N.; Guo, J.; Chang, C. L. Effects of High Energy Au-ion Irradiation on the Microstructure of Diamond Films. *J. Appl. Phys.* **2013**, *113*, No. No. 113704.
(32) Chen, L.; Shet, S.; Tang, H.; Wang, H.; Deutsch, T.; Yan, Y.; Turner, J.; Al-Jassim, M. Electrochemical Deposition of Copper Oxide Nanowires for Photoelectrochemical Applications. *J. Mater. Chem.* **2010**, *20*, 6962−6967.
(33) Politano, A.; Chiarello, G. Electronic Properties of Gold Thin Films Studied by Electron Energy Loss Spectroscopy. *Gold Bulletin* **2009**, *42*, 195−200.
(34) Prawer, S.; Peng, J. L.; Orwa, J. O.; McCallum, J. C.; Jamieson, D. N.; Bursill, L. A. Size Dependence of Structural Stability in Nanocrystalline Diamond. *Phys. Rev. B* **2000**, *62*, R16360−R16363.
(35) Sankaran, K. J.; Panda, K.; Sundaravel, B.; Chen, H. C.; Lin, I. N.; Lee, C. Y.; Tai, N. H. Engineering the Interface Characteristics of Ultrananocrystalline Diamond Films Grown on Au-Coated Si Substrates. *ACS Appl. Mater. Interfaces* **2012**, *4*, 4169−4176.
(36) Jiang, L.; Yang, T.; Liu, F.; Dong, J.; Yao, Z.; Shen, C.; Deng, S.; Xu, N.; Liu, Y.; Gao, H. J. Controlled Synthesis of Large-Scale, Uniform, Vertically Standing Graphene for High-Performance Field Emitters. *Adv. Mater.* **2013**, *25*, 250−255.
(37) Calderazzo, F. Organometallic Derivatives of Palladium, Platinum, And Gold. *J. Organomet. Chem.* **1990**, *400*, 303−320.